

Single-Step Additive Manufacturing of Monolithic MXene Architectures for Integrated Wireless Energy Storage in Wearable Electronics

Zhen You, Yuzhe Chen, Xiaoyuan Jia, Xueqing Chen, Xuan Zhang, Qixiang Wang, Ning Ding, Shujuan Liu, Weiwei Zhao,* and Qiang Zhao*



Cite This: *ACS Appl. Nano Mater.* 2025, 8, 20540–20552



Read Online

ACCESS |

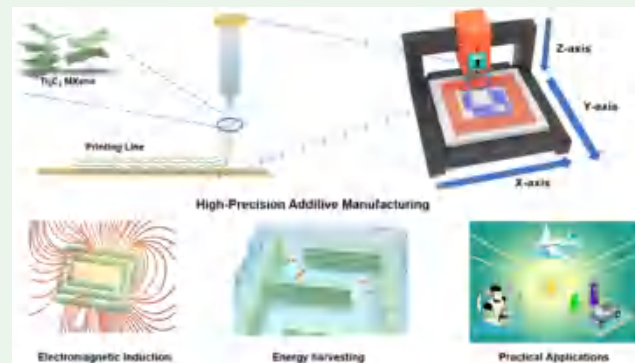
Metrics & More

Article Recommendations

Supporting Information

ABSTRACT: Flexible energy storage devices with integrated wireless charging units enable compact, mobile power solutions for next-generation wearable electronics. However, conventional multistep hybrid fabrication processes often suffer from interfacial energy losses and limited mechanical flexibility, hindering seamless integration. Here, we present a single-step extrusion printing strategy utilizing rheologically tailored Ti_3C_2 MXene inks to simultaneously print interdigitated microsupercapacitors (MSCs) and wireless charging coils. This approach leverages shear-aligned MXene nanochannels to construct bifunctional modules that achieve 51.9% wireless power transfer efficiency, high areal capacitance (59.36 mF cm^{-2}), and high energy density ($26.71 \mu\text{Wh cm}^{-2}$), effectively addressing traditional interfacial limitations. The integrated device exhibits excellent mechanical robustness, maintaining capacitance stability under various bending angles or 10,000 folding cycles. Following only 8 min of wireless charging, it delivers a peak power output of 1.3 mW, outperforming existing planar MSCs. Notably, a 140 s charging period enables continuous operation of a humidity and temperature sensor for 43 min, setting a record-high charge-to-use ratio of 18.4. This study establishes a groundbreaking paradigm for seamless wireless power-storage integration that offers transformative design principles and fabrication strategies for next-generation wearable electronics.

KEYWORDS: MXene, additive manufacturing, wireless energy storage, integrated system, wearable electronics



1. INTRODUCTION

The rapid development of wearable and implantable electronics has intensified the demand for miniaturized, flexible, and self-sufficient energy storage systems that can operate without wired recharging.^{1,2} Among diverse energy storage devices, microsupercapacitors (MSCs) have emerged as highly promising candidates due to their high power density, fast charge/discharge rates, and long cycle life.^{3–5} Although their integration with wireless charging modules presents a promising pathway toward self-powered systems through the principles of electromagnetic induction and magnetic resonance, they still face critical challenges.^{6–8} (i) Rigid coils are typically incompatible with soft substrates and flexible electrodes, leading to mechanical delamination and interfacial losses that reduce stability and device lifespan.^{9,10} (ii) Existing subtractive manufacturing methods (e.g., photolithography and laser ablation) suffer from material waste and limited resolution, severely constraining device scalability.^{11–13} (iii) Most flexible wireless power transfer (WPT) systems have an efficiency of less than 30% due to the significant impact of alignment, distance, and displacement on performance, making

it difficult to provide power to electronic devices for an extended period.¹⁴ Therefore, significant challenges remain in exploring novel flexible materials and simplified additive manufacturing to fulfill the stringent requirements of seamless wireless energy storage devices.^{15–18}

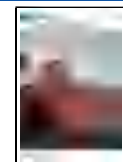
MXene, as a family of two-dimensional (2D) transition metal carbides/carbonitrides, has emerged as a cutting-edge material for energy storage and wireless transmission applications due to its high electrical conductivity ($2 \times 10^5 \text{ S cm}^{-1}$), mechanical flexibility, superior electrochemical performance, and unique electromagnetic properties.^{19–22} To date, the significant advancements in wireless charging technology have exploited these attributes through a well-designed architectures.^{17,23} For instance, Wu et al. demon-

Received: August 20, 2025

Revised: September 29, 2025

Accepted: October 4, 2025

Published: October 13, 2025



strated an all-in-one MXene-based wireless charging microsystem by integrating receiver coils with parallel MSCs, achieving remarkable energy transmission efficiency.²⁴ However, the existing MXene-based devices rely on a complex multistep fabrication process including MXene film filtration, transfer protocols, and ultraviolet laser etching methods.^{25,26} These complex multistep processes pose challenges in terms of scalability and cost-effectiveness, potentially introducing interfacial losses.²⁷ In contrast, extrusion printing technology, as one of the prominent additive manufacturing techniques, offers a transformative alternative by enabling high-precision, direct deposition of MXene inks.^{28–30} It facilitates the rapid and customizable fabrication of devices.^{31,32} This method streamlines the manufacturing process by eliminating intermediate steps, thereby significantly improving production scalability without compromising functional precision.^{33,34} To date, no study has reported the use of MXene's multifunctional properties combined with the additive manufacturing advantages of extrusion printing to address the integration challenges in wireless power systems.

In this work, we pioneer a single-step additive manufacturing platform of extrusion printing for monolithic MXene architectures that seamlessly integrates wireless coils with microsupercapacitors (IWC-MSCs).³⁵ It effectively addresses two fundamental challenges in conventional systems. (i) The seamless single-step extrusion printing of wireless coils and interdigitated electrodes eliminates interfacial resistance and mitigates mechanical mismatch.³⁶ (ii) An optimal electromagnetic coupling design achieves 51.9% energy transfer efficiency, which reduces power losses in traditional wireless systems. The IWC-MSCs exhibit exceptional performance metrics, including a high areal capacitance of 59.36 mF cm⁻² (1.8 V window), an enhanced energy density of 26.71 µWh cm⁻², and remarkable cycling stability. The devices maintain excellent mechanical durability, with nearly 100% capacitance retention after 10,000 bending-recovery cycles at 90°. Furthermore, this interface-free IWC-MSC system integrates seamlessly with wearable supports and operates a humidity and temperature sensor for 43 min on a single charge. Our work establishes a transformative IWC-MSCs platform that bridges advanced material innovation with scalable manufacturing for next-generation flexible electronics.

2. EXPERIMENTAL SECTION

2.1. Materials. Ti₃AlC₂ MAX powder (99.99 wt %) was purchased from 11 Technology Co., Ltd. (Jilin, China). LiF (99 wt %) was purchased from Aladdin Biochemical Technology Co., Ltd. Hydrochloric acid (HCl) solution was purchased from Nanjing Chemical Reagent Co., Ltd. Flexible transparent poly(ethylene glycol) terephthalate (PET) substrates were purchased from Hengda Automation Technology Co., Ltd. (Taizhou, China). A commercially available temperature and humidity sensor module was purchased from Shenzhen Xuantejia Electronics Co., Ltd. and directly used for integration and demonstration. All materials in this work were used as received without further purification.

2.2. Characterization. SEM image was characterized by scanning electron microscopy (FESEM, Hitachi S-4800). TEM image was recorded by transmission electron microscopy (Hitachi HT7700). XRD pattern was carried out by an X-ray diffractometer (Bruker AXS D8 Advance), using Cu Kα radiation ($\lambda = 1.5406 \text{ \AA}$) over the range of $2\theta = 5.0\text{--}60.0^\circ$. Thin-film sheet resistance was tested by a dual electric digital four-probe tester (ST2263, China). A rheometer (Discovery HR 30) was used for characterizing the rheological properties of the ink. A dual electronic digital four-probe tester (ST2263, China) was employed to measure the sheet resistance of the

thin films. Cyclic voltammetry, galvanostatic charge–discharge tests, and electrochemical impedance spectroscopy (EIS) measurements were conducted by using an electrochemical workstation (CHI 660E, Shanghai Chenhua Instrument Co., Ltd.). All tests were performed under a two-electrode system.

2.3. Preparation of Ti₃C₂ MXene Inks. First, LiF (0.5 g) was dissolved in HCl (7.5 mL, 9 M). The commercial Ti₃AlC₂ bulk (0.5 g) was slowly added to the mixture and kept at 60 °C for 24 h. The products were washed with deionized water five times until the pH was above 6. The samples were dried under vacuum for 12 h. Then, m-Ti₃C₂ bulks (300 mg) were dispersed in 30 mL of deionized water and sonicated (60 kHz, 360 W) for 1 h. The dispersion was centrifuged at 3500 rpm for 1 h; 80% of the upper solution was sucked up to discard the unexfoliated m-Ti₃C₂. Finally, the supernatant was centrifuged at 6000 rpm for 1 h, and the precipitate obtained was a Ti₃C₂ MXene inks. To ensure environmental safety and regulatory compliance, all waste liquids generated during the MXene synthesis are collected in a dedicated chemical waste container and are handled by a certified solid waste disposal company. The disposal process strictly follows relevant national standards and environmental regulations of China.

2.4. High-Precision Printing Technology. The printing system employs two positioning points to fix the substrate on the platform and establish a two-dimensional coordinate system; the first point is designated as the origin. The thickness of the Ti₃C₂ MXene conductive pattern is regulated by three key factors: the extrusion pressure of the dispensing machine (printing pressure), the z-axis distance (printing height), and the speed of both the x- and y-axis (printing speed) managed by the mechanical arm. Additionally, a laser rangefinder is integrated into the printer to accurately measure the z-axis distance prior to printing. This z-axis distance measurement and calibration against the reference plane enable the printing of Ti₃C₂ MXene components with a smooth surface. To obtain interdigital electrodes and the WCC pattern, the parameters are set to 35 kPa for pressure, 15 mm s⁻¹ for velocity, and 0.46 mm for height.

2.5. Preparation of IWC-MSCs. To prepare the gel electrolyte, 1 g of PVA was dissolved in 10 mL of deionized water, followed by the gradual addition of 0.55 mL of H₂SO₄ with continuous stirring. The mixture was heated at 90 °C for 2 h to obtain a homogeneous PVA/H₂SO₄ gel electrolyte. After the mixture was cooled to room temperature, the prepared gel electrolyte was carefully drop-cast between the MSC electrodes (excluding the Ti₃C₂ MXene WCCs). A second PET tape was then placed on top of the entire device to encapsulate the structure.

2.6. Encapsulation and Accelerated Aging Test. The IWC-MSCs were encapsulated using a PET sealing layer and stored in a temperature–humidity chamber at 60 °C and 90% relative humidity (RH) for 7 days. Electrochemical performance was evaluated before and after the test by cyclic voltammetry (CV, 500 mV s⁻¹).

2.7. Mechanical Flexibility Test. The mechanical durability of the IWC-MSCs was evaluated through cyclic bending at a fixed angle of 90° for 10,000 cycles. The test sample had a lateral arc length of 31.8 mm. According to the geometric relation

$$r = \frac{L}{\theta} \quad (1)$$

where $L = 31.8 \text{ mm}$ and $\theta = 90^\circ = \pi/2 \text{ radians}$, the corresponding bending radius r is calculated as 20.2 mm. This condition represents a realistic and moderate mechanical deformation scenario.

2.8. Electrochemical Measurements. All electrochemical measurements were performed using a two-electrode configuration under ambient conditions. The areal capacitance, energy density, and power density were calculated based on the geometric area of the single-layer-printed MSCs and four-layer-printed MSCs. The areal capacitance (C_A) was calculated using either galvanostatic charge–discharge (GCD) or cyclic CV according to the following equations:³⁷

From GCD

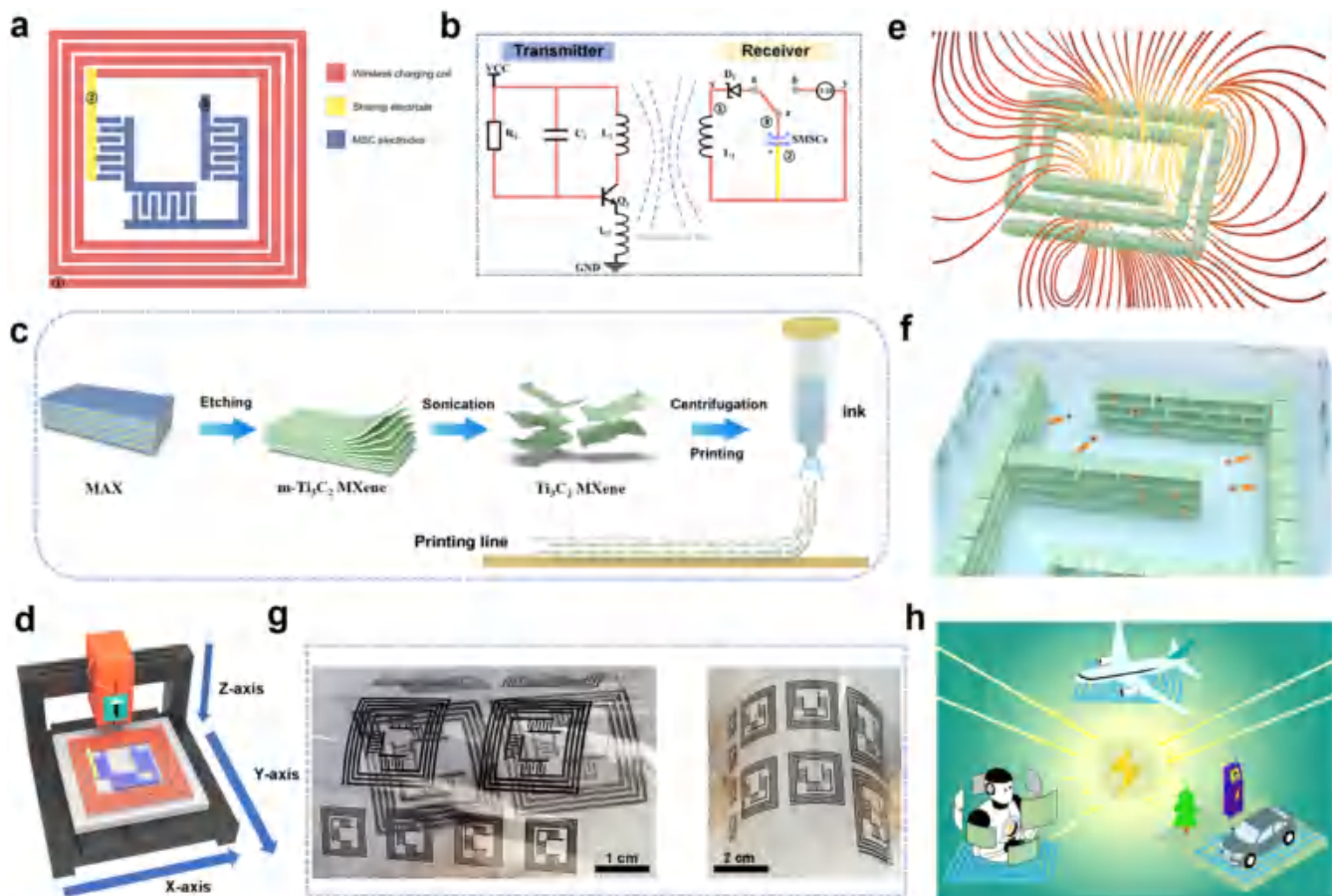


Figure 1. (a) Schematic diagram of IWC-MSCs. (b) Circuit diagram of wireless transmitter and receiver. (c) Schematic diagram of the preparation process for Ti_3C_2 MXene nanosheets and inks. (d) Diagram depiction of a microelectronic printer. (e) Schematic illustration of magnetic field distribution in printed coils. (f) Schematic illustration of ion diffusion within the Ti_3C_2 MXene nanochannels. The diagram depicts the layer-by-layer arrangement of the Ti_3C_2 MXene nanosheets. (g) (i) Local structure and (ii) overall view of the IWC-MSCs array under flexible states. The IWC-MSCs of various sizes can be directly patterned onto PET substrates. (h) Conceptual schematics of potential application scenarios including wearable sensors, electric vehicles, and aerospace electronics.

$$C_A (\text{F cm}^{-2}) = \frac{I (\text{A}) \times \Delta t (\text{s})}{\Delta V (\text{V}) \times A (\text{cm}^2)} \quad (2)$$

From CV

$$C_A (\text{F cm}^{-2}) = \frac{1}{V \times (V_h - V_l) \times A} \int_{V_l}^{V_h} I(V) dV \quad (3)$$

where C_A , I , Δt , ΔV , and A are the areal capacitance (F cm^{-2}), charge/discharge current (A), discharge time (s), discharge voltage (V), and the area of the electrode (cm^2), respectively. V is the scanning rate of CV curves (V s^{-1}); V_h and V_l are the highest and lowest voltages of the potential window (V), respectively. A is the area of electrodes (cm^2) and C_A is the integrated area of the CV curves.

Calculation of energy density and power density³⁸

$$E (\text{Wh cm}^{-2}) = \frac{I (\text{A}) \times \int_{t_b}^{t_c} V(t) dt}{A (\text{cm}^2) \times 3600} \quad (4)$$

$$P (\text{W cm}^{-2}) = \frac{E (\text{Wh cm}^{-2})}{\Delta t (\text{s})} \times 3600 \quad (5)$$

where E is the energy density (Wh cm^{-2}), P is the power density (W cm^{-2}), t_b and t_c are the beginning and ending times of discharging, respectively; V is the device voltage; and A is the integrated area from the galvanostatic discharging curves. The induced electric charge (Q) of WCC in IWC-MSCs after wireless charging was calculated by

$$Q (\text{mC}) = \int_{t_B}^{t_E} I(t) dt \quad (6)$$

where t_B and t_E are the beginning and ending times of wireless charging, respectively; I is the induced current by wireless charging coils (WCC) at real-time; and Q is the integrated area from induced current curves. The EIS measurements were conducted in the frequency range of 0.1 Hz to 1 MHz with 5 mV of amplitude.

The power transfer efficiency (PTE) is calculated as⁴⁴

$$\text{PTE} = \frac{P_{\text{out}}}{P_{\text{in}}} \times 100\% \quad (7)$$

where P_{in} and P_{out} represent the input power from the transmitter and the output power received by the load (the microsupercapacitor), respectively.

3. RESULTS AND DISCUSSION

3.1. Design and Fabrication of Flexible IWC-MSCs.

The IWC-MSCs device integrates two primary components: the WCC, which operates as an antenna, and the MSCs, which serve as energy storage devices (Figure 1a).³⁹ The charging principle is based on Faraday's law of electromagnetic induction (Figure 1b).⁴⁰ The wireless energy transfer system consists of a transmitter (Tx) and a receiver (Rx) and operates via inductive coupling to deliver energy wirelessly to flexible electronic devices. The Tx unit is composed of a negative-

positive-negative (NPN) small-signal transistor (Q1), inductors L1 and L2, capacitor C1, and bias resistor R1. This configuration generates an alternating magnetic field via coil L1. The Rx unit includes a receiving coil (L3), a rectifier diode (D1), MSCs, a temperature–humidity sensor, and a mode-select switch (a-z-b). It is responsible for capturing, rectifying, storing, and using the transmitted energy. The working mechanism follows these steps. (i) Reception and rectification (a-z mode). Magnetic coupling between coils L1 (Tx) and L3 (Rx) induces an alternating current (AC) voltage in L3 (Figure 1e).^{7,41} This alternating voltage is rectified by diode D1 and subsequently charges the MSCs, thus completing wireless energy reception and storage. The charging process is further illustrated in Figure 5d, which shows the voltage across the MSCs increasing while the current gradually decreases during wireless charging, reflecting the energy accumulation in the capacitors. (ii) Energy utilization (b-z mode). When the switch is flipped to b-z, the stored energy in the MSCs is used to power the temperature–humidity sensor. This enables real-time energy utilization and indicates the energy storage state. Figure 5e presents the discharging process, where both the voltage and the current decrease over time, demonstrating controlled energy release. To achieve efficient inductive coupling and compact integration, the IWC-MSCs adopt a regular planar structure. To achieve efficient inductive coupling and compact integration, the IWC-MSCs adopt a regular planar structure. In this structure, the MSCs are centrally located and are surrounded by the receiving coils (Figure 1a). An electrode (marked by a yellow dotted line in Figure 1a) is shared by the MSCs (marked by the blue line in Figure 1a) and WCC (marked by the red line in Figure 1a). This electrode serves as a conductive line for the coils to harvest energy from the external magnetic field, as well as functions as an electrode for three interdigital MSCs in series. On this basis, two alternative configurations are further explored to evaluate their effects on device performance (Figure S1). In the first structure, all four sides of a square layout are utilized as electrodes for four parallel MSCs (Figure S1a). This configuration forms a new closed-loop coil, generating a magnetic field similar to that of the peripheral WCC. However, the induced magnetic field may interfere with the potential difference across the MSC electrodes and negatively impact their charge storage capacity. In the second design, a U-shaped shared electrode is introduced to connect the MSCs and the WCC (in Figure S1b). While this configuration supports wireless energy reception, the parallel MSCs share the same voltage window as a single unit, which limits their ability to drive higher-voltage devices.⁴² In contrast, the optimized IWC-MSCs design effectively overcomes these limitations. By arranging three MSCs in series at the center of the planar structure and surrounding them with the WCC, the device achieves both high energy density and seamless wireless charging integration.¹⁴ Moreover, the deliberate spacing around the MSCs, instead of fully occupying the central area, minimizes magnetic interference, further enhancing the overall system performance. The improved electromagnetic coupling structure enhances magnetic field-to-electric energy conversion and reduces eddy current losses and resistive heating, thereby lowering overall power loss (Figure S2).

Besides rigorous structural design, the selection of flexible materials and high-precision fabrication technology also play a crucial role in obtaining high-integrity IWC-MSCs.⁴³ In conventional WCC, to ensure effective current transport in

practical antenna applications, the coil resistance is strictly required to be maintained below $1 \Omega \text{ m}^{-1}$.⁴⁴ To meet this critical requirement, 2D ultrathin Ti_3C_2 MXene nanosheets are employed as both WCC and electrode current collectors due to their high electrical conductivity, exceptional mechanical flexibility, lightweight quality (3.62 g cm^{-3}) and low-heat generation.^{45,46} They can be prepared through selectively etching the Al layers from Ti_3AlC_2 MAX bulks and subsequently exfoliating the resulting multilayered Ti_3C_2 (m- Ti_3C_2) MXene bulks (Figure 1c). The corresponding XRD patterns show the disappearance of the characteristic Ti_3AlC_2 (002) peak and the shift of the (002) reflection for m- Ti_3C_2 , confirming successful etching of Al layers and the formation of multilayered Ti_3C_2 MXene (Figure S3). Initially, the additive-free Ti_3C_2 MXene inks are prepared via centrifugal concentration. Here, “additive-free” refers to the absence of any external surfactants, polymers, or dispersants in the ink formulation. The surface functional groups ($-\text{F}$, $-\text{OH}$, and $-\text{O}$) are intrinsic to the MXene structure and originate naturally from the etching process. To further eliminate residual ionic species such as Li^+ / F^- / H^+ / Cl^- , repeated centrifugation and washing steps are conducted. The effectiveness of this purification is confirmed by X-ray photoelectron spectroscopy (XPS). As shown in Figure S4a, the survey scan of Ti_3C_2 displays distinct Ti, C, and F signals with no detectable Li or Cl. Further high-resolution spectra of F 1s (Figure S4b) and the O 1s (Figure S4e) validate the successful removal of impurities. This ensures the long-term rheological and electrochemical stability of the inks for precise extrusion printing. These inks are then employed in a microelectronic printer to fabricate seamlessly integrated IWC-MSCs in one-step operation (Figure 1d).⁴⁷ During the printing process, shear forces along the axial direction of the printing head induce the alignment of Ti_3C_2 MXene nanosheets, resulting in densely stacked, well-aligned, and interconnected flakes parallel to the substrate. The Ti_3C_2 MXene-based layer exhibits high electrical conductivity and a 2D lamellar structure, which contribute to efficient inductive coupling and energy harvesting during wireless charging (Figure 1e).⁴⁸ To better illustrate the charge storage mechanism, a schematic diagram is provided in Figure 1f. The Ti_3C_2 MXene nanosheets are envisioned to self-assemble into a layer-by-layer structure, forming well-aligned interlayer nanochannels. These nanochannels serve as efficient ion diffusion pathways, allowing electrolyte ions to access electroactive surfaces rapidly and uniformly. This structural feature has been widely reported to enhance both the capacitance and rate performance of MXene-based supercapacitors.^{19,49} Figure 1g presents both the local structure and the overall view of the IWC-MSCs array under bending, demonstrating its mechanical flexibility. The devices of various sizes are directly patterned onto PET substrates, confirming the scalability of the printing process. Figure S5 further illustrates that patterns with customizable shapes and sizes can be directly printed on PET substrates by changing the printing parameters, highlighting the adaptability of the fabrication process and supporting integration into flexible electronic systems. To envision the broader impact of IWC-MSCs, a conceptual schematic is presented in Figure 1h, illustrating potential application scenarios, such as wearable health monitoring, self-charging electric vehicles, and lightweight aerospace power modules. These future directions leverage the device’s structural flexibility, mechanical durability, and scalable fabrication process, making it a promising candidate

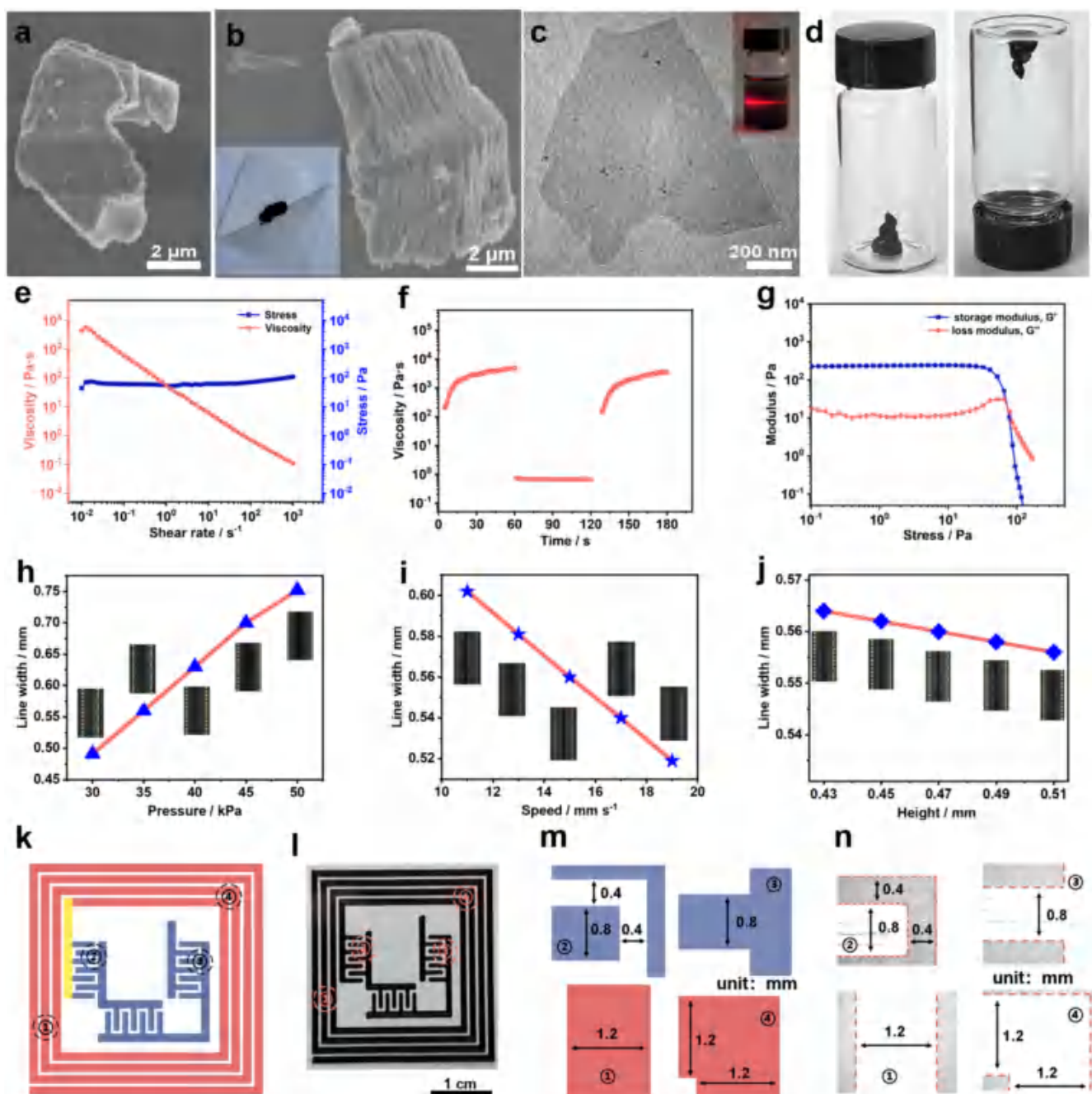


Figure 2. (a, b) SEM image of the commercial Ti_3AlC_2 MAX bulks and m- Ti_3C_2 MXene bulks. Inset: Photograph of the m- Ti_3C_2 MXene powders. (c) TEM image of the Ti_3C_2 MXene nanosheets. Inset: Photograph of the Tyndall effect for the Ti_3C_2 MXene colloids. (d) Photograph of Ti_3C_2 MXene inks of 60 mg mL^{-1} . (e, f) Viscosity of the Ti_3C_2 MXene inks as a function of shear rate, shear stress, and interval shearing time. (g) Storage and loss modulus of Ti_3C_2 MXene inks as a function of shear stress. Effects of printing parameters on the line width of Ti_3C_2 MXene lines including extrusion pressure (30–50 kPa) (h), printing speed (11–19 mm s⁻¹) at 35 kPa and 0.47 mm height (i), and printing height (0.43–0.51 mm) at 35 kPa and 15 mm s⁻¹ (j). Line width increases with pressure, decreases with speed, and slightly decreases with height. (k, l) Graphic design and photograph of the IWC-MSCs. (m, n) Comparison of theoretical design values and measured values.

for real-time, on-demand wireless energy harvesting in space-constrained and dynamic environments. (Figure 1h).^{50–52}

3.2. High-Precision All-MXene-Printed IWC-MSCs. The fabrication of additive-free MXene inks is important to achieve high-precision patterning capabilities and biocompatible interfaces in IWC-MSCs for the application of wearable electronics.^{23,53} The commercial Ti_3AlC_2 MAX phase has an average particle size of $\sim 38 \mu\text{m}$ (Figure 2a). Scanning electron microscopy–energy-dispersive spectroscopy (SEM-EDS) map-

ping reveals a uniform distribution of Ti, Al, and C elements (Figure S6a). After the Al atomic layer is selectively etched away, the accordion-like m- Ti_3C_2 MXene bulks are obtained with expanded interlayer spacing (Figure 2b). SEM-EDS mapping reveals a uniform distribution of Ti, C, O, and F elements (Figure S6b). Next, the Ti_3C_2 MXene nanosheets with the lateral dimension of $1 \mu\text{m}$ are produced through subsequent liquid-phase exfoliation under ultrasonication (Figure 2c). Through further centrifugal concentration, the

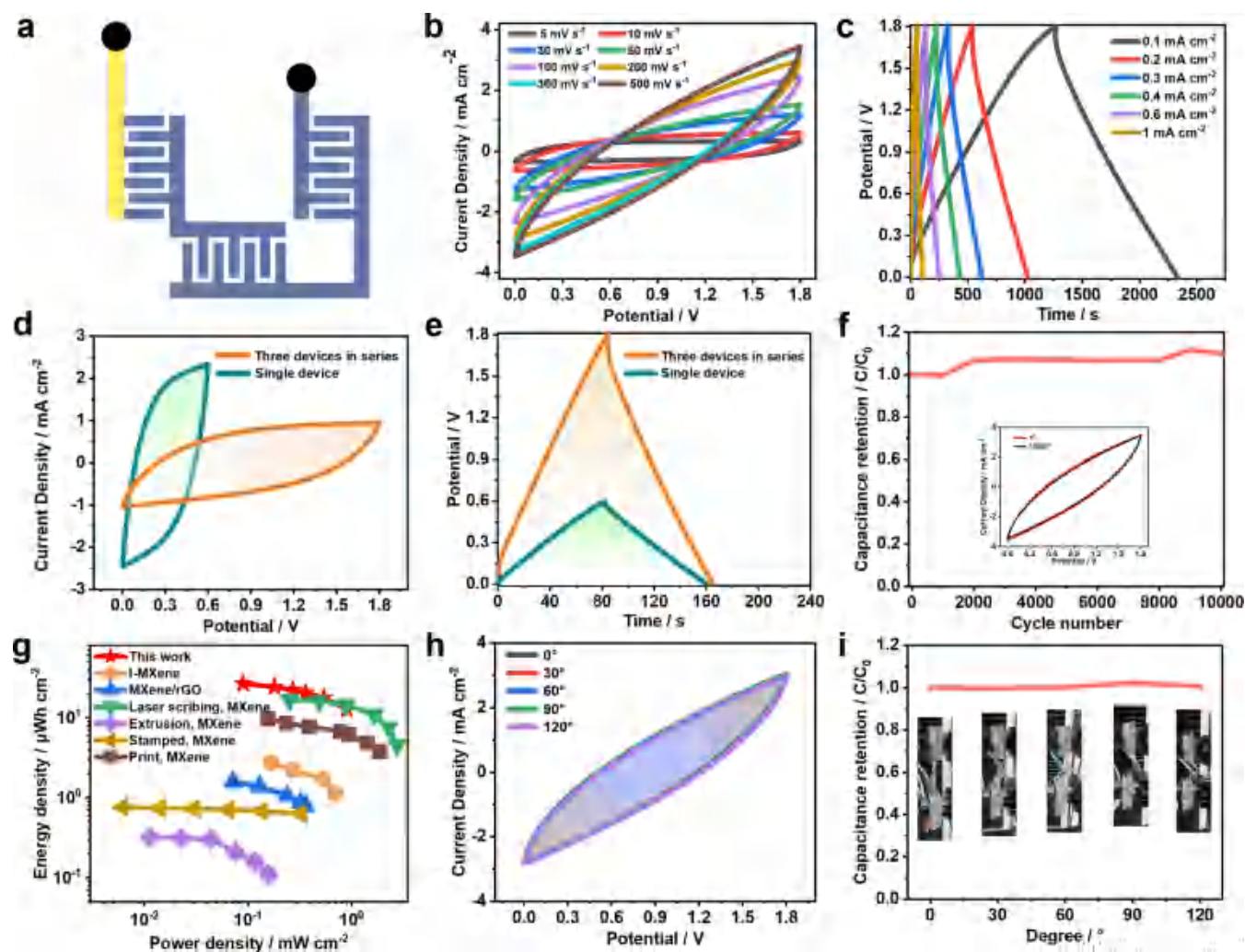


Figure 3. (a) Schematic diagram of three MSCs in series. (b) CV curves at different scanning rates. (c) GCD curves at different current densities. (d) CV curves of single-layer-printed MSCs measured at scan rates of 100 mV s^{-1} . (e) GCD curves of single-layer-printed MSCs at the current density of 0.2 mA cm^{-2} . Capacitance retention of the MSCs during 10,000 charge–discharge cycles (f) and Ragone plots compared with other reported MSCs (g) of three four-layer-printed MSCs in series. CV curves (h) and capacitance retention (i) at different bending angles of 0, 30, 60, 90, and 120° at 300 mV s^{-1} . Inset: The corresponding photographs.

additive-free Ti_3C_2 MXene inks exhibit a high concentration of 60 mg mL^{-1} (Figure 2d). The colloidal stability of the inks benefits from the synergistic effects of abundant surface-terminated hydrophilic groups (i.e., $-\text{F}$, $-\text{OH}$, and $-\text{O}$).⁵⁴ Figure 2e shows the viscosity and shear stress of the Ti_3C_2 MXene inks as a function of shear rate, which varies between 0.01 s^{-1} and 100 s^{-1} to simulate the extrusion process. As the shear rate increases, the formulated inks display favorable shear-thinning viscoelastic properties with a viscosity of 2.5×10^2 Pa·s, enabling continuous extrusion and rapid solidification. Figure 2f presents the viscosity of the Ti_3C_2 MXene inks as a function of the interval shear time. The viscosity of the inks can be instantly switched between shear rates of 0.01 and 100 s^{-1} . Figure 2g compares the storage modulus (G') and loss modulus (G'') of Ti_3C_2 MXene aqueous inks versus shear stress. At low shear stress, G' and G'' remain relatively stable with $G' > G''$, indicating elastic-dominated behavior during deformation and reflecting the material's solid-like characteristics.²³ When the shear stress reaches the critical value, G' and G'' converge to equal magnitudes, marking the critical transition point from an elastic to viscous-dominated response. Beyond this threshold, the material initiates flow with $G'' > G'$,

demonstrating viscous-dominated behavior characteristics of fluid-like properties.⁵⁵ Consequently, the tunable rheological properties of the as-formulated Ti_3C_2 MXene inks appropriately ensure stability and quality in the extrusion printing process.

The employed high-precision extrusion printing system integrates two core subsystems, including a three-axis motion control platform (X-axis, Y-axis, and Z-axis) and a high-definition machine vision-based optical alignment module (Figure 1d). This integration enables the direct fabrication of Ti_3C_2 MXene patterns. To ensure precise deposition of customized patterns under programmable control, the dependence of the line width on key parameters such as pressure (p), speed (v), and printing height (h) is systematically investigated. We also quantitatively characterize the correlations among these parameters to establish predictive models for fidelity optimization of the printed patterns. The effect of pressure on the line width and surface topography of the Ti_3C_2 MXene lines is first explored under specific conditions where $v = 15 \text{ mm s}^{-1}$ and $h = 0.47 \text{ mm}$. As illustrated in Figure 2h, when the pressure is set as 30, 35, 40, 45, and 50 kPa, the measured line widths are 0.49, 0.56, 0.63, 0.70, and 0.75 mm,

respectively. As the pressure increases, the line width expands. This phenomenon can be ascribed to the fact that a higher pressure leads to an increased extrusion volume of Ti_3C_2 inks per unit time. The lowest pressure threshold for the printing system is determined to be 30 kPa. After a comprehensive consideration, 35 kPa is selected as the optimal pressure value. This choice allows for a balance between the printing resolution and the uniformity of the printed lines. The influence of printing speed on the line width of the Ti_3C_2 MXene lines is subsequently investigated under certain parameters of $p = 35$ kPa, and $h = 0.47$ mm (Figure 2i). The measured line widths are 0.60, 0.58, 0.56, 0.54, and 0.52 mm at printing speeds of 11, 13, 15, 17, and 19 mm s^{-1} , respectively. As the printing speed increases, the line width decreases, which improves the printing resolution because less Ti_3C_2 MXene ink is deposited per unit time. Printing efficiency determines the overall printing time of the device. A higher printing speed leads to a greater efficiency. As the printing speed increases from 11 to 15 mm s^{-1} , the edge flatness of the Ti_3C_2 MXene line remains well preserved. However, when the printing speed is further increased from 15 to 19 mm s^{-1} , the edge flatness of the Ti_3C_2 MXene line deteriorates due to insufficient Ti_3C_2 MXene ink deposition. Accordingly, a printing speed of 15 mm s^{-1} is selected as an optimal condition to balance printing efficiency, resolution, and the edge flatness of the Ti_3C_2 MXene lines. Finally, the printing height, which is defined as the distance between the nozzle and the substrate, is investigated under certain parameters of $v = 15$ mm s^{-1} and $p = 35$ kPa. The relationship between the line width and printing height is presented in Figure 2j. The line width is measured as 0.564, 0.562, 0.560, 0.558, and 0.556 mm for the printing height of 0.43, 0.45, 0.47, 0.49, and 0.51 mm, respectively. When the nozzle tip height falls below the critical threshold of 0.45 mm, physical contact with the substrate occurs, inducing tip deflection and potential structural damage. Conversely, the excessive nozzle-substrate distance prevents timely ink-substrate adhesion, resulting in ink coalescence at the nozzle orifice. This accumulation persists until gravity overcomes surface tension, leading to intermittent droplet release that deviates from the intended computer-aided design (CAD) patterns. Consequently, a printing height of 0.47 mm is chosen for the subsequent experiments.

The seamless IWC-MSCs device consists of three interdigital MSCs connected in series (located at the center of the device) and WCC (positioned on the outside of the device) with a specific number of 4 turns (Figure 2k). The Ti_3C_2 MXene lines are printed on plasma-treated PET substrate using the optimal printing parameters of $v = 15$ mm s^{-1} , $p = 35$ kPa, and $h = 0.47$ mm. Through a one-step printing process, the MSCs and WCC are seamlessly integrated, effectively minimizing the interconnect length and ensuring low resistance throughout the device (Figure 2l). Uniform system integration reduces interference and energy loss while enhancing component compatibility and synergy, thereby improving the long-term flexibility of the device.⁵⁶ The theoretical dimensions of the local regions in the CAD drawing are illustrated in Figure 2m. The corresponding high-resolution optical photos are taken by the microelectronic printer's camera (Figure 2n). The printed lines and angles feature clear and smooth edges that closely align with the theoretical values, demonstrating the high-precision advantages of the printing technology.

3.3. Electrochemical Performance of Flexible MSCs.

The electrochemical performance of three MSCs connected in series is evaluated through electrochemical characterization (Figure 3a). The $\text{H}_2\text{SO}_4/\text{PVA}$ gel electrolyte is selected as the electrolyte. The MSCs are encapsulated with a PET sealing layer to mitigate air exposure and electrolyte leakage. For interdigitated MSCs, the finger spacing (d) critically influences the capacitance characteristics by modulating the electric field distribution and, consequently, the overall electrochemical performance.⁵⁷ According to the basic formula of a parallel-plate capacitor $C = \epsilon A/d$ (where ϵ is the permittivity, A is the electrode area, and C is the capacitance value), the capacitance of interdigitated MSCs is closely related to the value of d .⁵⁸ As d decreases, it is equivalent to reducing the effective plate-to-plate distance. An increase in the dielectric constant (ϵ) or effective electrode area (A) enhances the capacitance (C), which improves the charge storage and release capabilities of the supercapacitors during cycling, thereby optimizing their electrochemical performance. Accordingly, the influence of d (i.e., 0.4, 0.8, and 1.2 mm) on the electrochemical performance is first explored for single-layer-printed MSCs (Figure S7). The experimental results clearly show that the electrochemical performance is increased from 21.35 and 25.90 to 27.85 mF cm^{-2} as the gap is decreased from 1.2 and 0.8 to 0.4 mm (Figure S8). Consistent with the theoretical analysis, a smaller electrode spacing (d) concentrates and homogenizes the electric field distribution within the MSCs, mitigates edge effects, and further improves capacitance characteristics as well as energy storage and conversion efficiency.^{59–61} However, excessively reducing the spacing (d) during printing increases fabrication difficulty and may cause line adhesion or short circuits, which severely compromises printing accuracy and device yield. Therefore, a spacing of 0.4 mm is selected as the optimal value. This choice, commonly adopted in related studies, provides a balance between device performance and fabrication feasibility.

For further practical applications of MSCs, we first investigated the effect of Ti_3C_2 MXene electrode thickness on device performance. When the number of printing layers is set to 1, 2, 3, and 4, the corresponding electrode thicknesses are set as 4, 8, 12, and 16 μm (Figure S9), and the sheet resistances are 365, 186, 116, and 81 $\text{m}\Omega \text{ sq}^{-1}$, respectively (Figure S10). In addition, as the thickness of the MXene electrode increases, the Ti_3C_2 MXene loading per unit area also increases, theoretically enhancing the areal capacitance of the Ti_3C_2 MSCs by storing more charge. Therefore, we measure the CV and GCD curves of the four-layer-printed MSCs (Figure 3b,c). To examine the scalability of the MSCs, three devices are connected in series. The series configuration yields a potential window three times that of a single MSC (Figure 3d,e), demonstrating the desirable tandem behavior of the fabricated MSCs.⁶² The areal capacitances of the four-layer-printed MSCs, calculated according to the current density, are 59.36, 53.93, 49.47, 45.84, 39.47, and 28.39 mF cm^{-2} at current densities of 0.1, 0.2, 0.3, 0.4, 0.6, and 1.0 mA cm^{-2} , respectively (Figure S11). The capacitance retention is 47.83% when the current density is increased by a factor of 10, indicating good rate performance. The device maintains nearly 100% capacitance retention after 10,000 charge–discharge cycles, demonstrating excellent electrochemical durability (Figure 3f). Moreover, at a bending angle of 90° (corresponding to a bending radius of 20.2 mm), the device maintains nearly 100% capacitance retention even after 10,000 CV cycles,

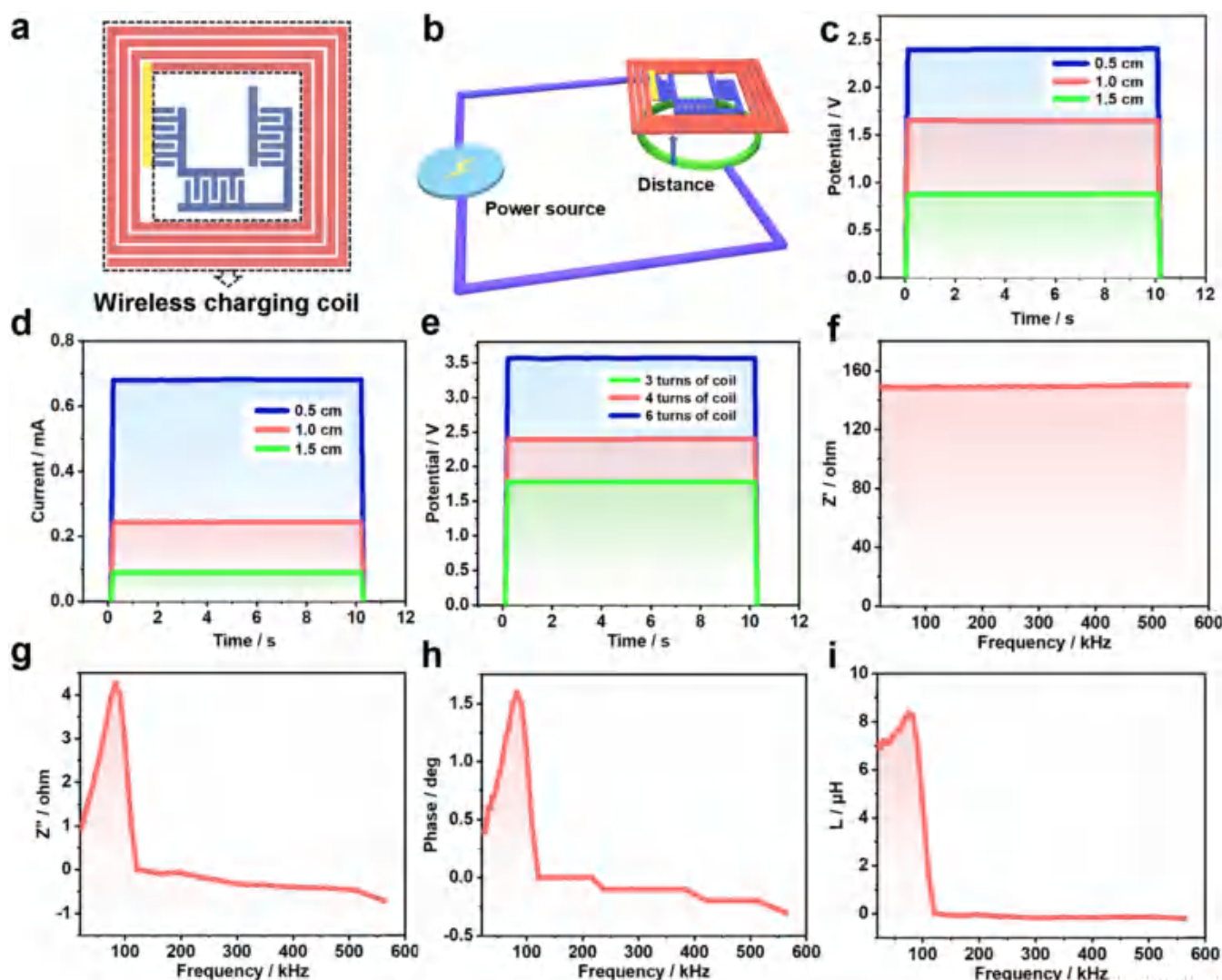


Figure 4. (a) Structure diagram of IWC-MSCs. (b) Charging diagram of the IWC-MSCs. (c) The received potential (c) and current (d) of WCC in IWC-MSCs under different distance to wireless transmitter during wireless charging process at the voltage source of 7 V. (e) Potential signals of WCC with 3, 4, and 6 turns of coils under the optimal distance of 0.5 cm. (f) Real impedance, (g) imaginary impedance, (h) phase, and (i) calculated inductance of WCC.

highlighting its remarkable mechanical flexibility and durability. (Figure S12) A gradual increase in capacitance is observed in the later stages of cycling (after several thousand cycles), which is likely attributed to the progressive activation of electrochemically accessible sites and structural reorganization at the MXene/electrolyte interface.⁶³ Based on the areal capacitance, the device delivers energy densities of 26.71 and 12.78 $\mu\text{Wh cm}^{-2}$ at power densities of 0.09 and 0.9 mW cm^{-2} , respectively (Figure 3g). These results are superior to the previously reported works (Table S1).^{64–66} The flexibility and electrochemical performance of the MSCs under mechanical deformation are evaluated by CV measurements at a scan rate of 300 mV s^{-1} under bending angles of 0, 30, 60, 90, and 120° (corresponding to bending radii of ∞ , 60.7, 30.4, 20.2, and 15.2 mm, respectively). As shown in Figure 3h, the CV curves exhibit good overlap at all bending states, indicating excellent mechanical flexibility. The corresponding capacitance retention is calculated and presented in Figure 3i, with the inset displaying the physical configurations of the device at each bending angle, further confirming its mechanical robustness.

The capacitance retention can also be well maintained at 97.13% over 30 days (Figure S13). It promotes practical potential as flexible capacitive energy storage devices as a power supply source. To assess the safety and durability of the electrolyte gel-based IWC-MSCs in practical applications, the devices are encapsulated with PET tape and subjected to accelerated aging tests at 60 °C and 90% RH for 7 days (Figure S14). The encapsulated devices retained 95.7% of their original capacitance with no signs of electrolyte leakage, delamination, or visual degradation (Figure S15). These results confirm the robust environmental stability of the device, supporting its potential for safe deployment in wearable electronics.

3.4. WCC Optimization of IWC-MSCs. As the antenna component of the IWC-MSCs, a narrower gap between adjacent coils improves signal output efficiency.¹⁴ A gap of 0.4 mm is set between adjacent coils, matching the finger spacing (*d*) in the MSCs (Figure 4a). The whole IWC-MSCs are functional as receivers (Figure 4b). For optimization of electrical energy harvesting from the magnetic field, the influence of key WCC parameters, including the receiving antenna distance, transmitter voltage, and the number of coil

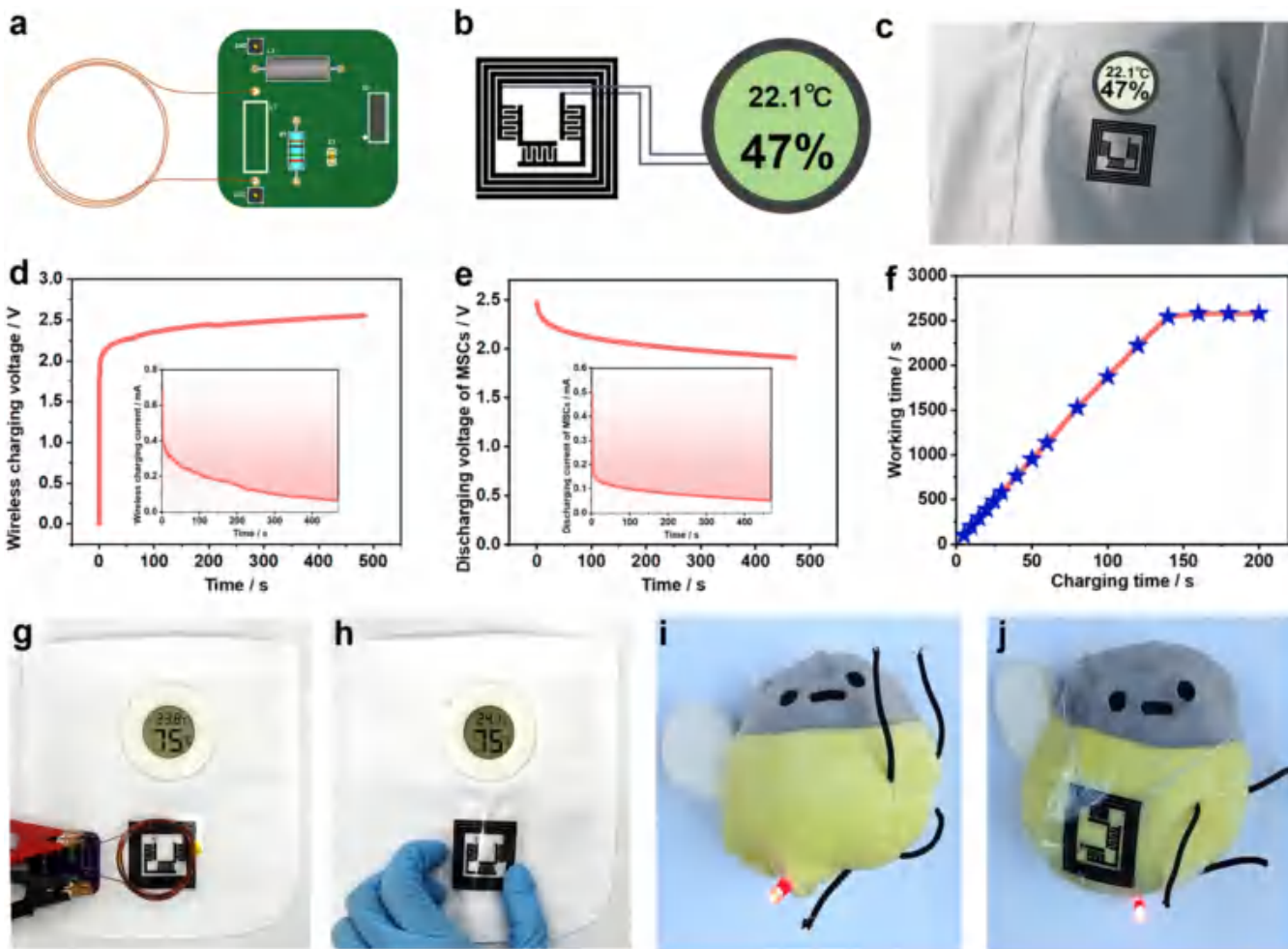


Figure 5. (a) Schematic diagram of the transmitter system. (b) Schematic illustration of the IWC-MSCs equipped with temperature and humidity sensors (based on actual photographs). (c) Application diagram of IWC-MSCs (illustrative drawing based on real-world implementation). Received voltage (d) and current (e) of the WCC in the IWC-MSCs were from the wireless transmitter under a 7 V power supply. (f) Correlation between wireless charging duration and working time. (g) IWC-MSCs integrated into a wearable temperature and humidity monitoring system. They are wirelessly charged via the printed coil and operates stably. (h) The wearable monitoring system remains functional under mechanical deformation, demonstrating the flexibility and operational stability of the IWC-MSCs. (i) IWC-MSCs embedded inside a doll provide power to a red LED, illustrating potential integration into soft or embedded electronics. (j) IWC-MSCs mounted on the surface of the doll also power the LED successfully, confirming their adaptability under different integration configurations.

turns, is systematically examined. First, the effect of the distance between antenna and power transmitter on wireless energy transfer is investigated with the transmitter voltage of 7 V. As the distance increases from 0.5, 1.0 to 1.5 cm, the output voltage of the receiver decreases from 2.4, 1.65 to 0.87 V, respectively (Figure 4c), and the output current decreases from 0.68 to 0.24 and 0.09 mA, respectively (Figure 4d and Table S2). As shown in Table S3, the wireless power transfer efficiency exhibits a strong dependence on the coil-to-coil distance. A 3D-printed fixture is employed to precisely control vertical alignment (Figure S16). The highest efficiency (51.9%) is achieved at 0.5 cm, while the efficiency sharply declines at distances beyond 1.0 cm and becomes negligible at 2.0 cm. These results highlight the critical impact of the magnetic coupling geometry in printed wireless systems. Furthermore, increasing the transmitter voltage to 10 V leads to a corresponding rise in both the output voltage and current of the receiving end (Figure S17 and Table S2). This is primarily attributed to the following reason. According to Faraday's law of electromagnetic induction, a stronger power

input to the primary coils leads to a greater rate of change in the magnetic field.⁵⁷ As the voltage of the power source at the transmitter increases, more energy is delivered to the transmitting coils, resulting in a higher charging current at the receiver. Consequently, the induced electromotive force in the secondary coils is also enhanced. Furthermore, the effect of coil turn number on wireless charging performance is investigated based on the controllable printing technique (Figure 4e). As the number of turns increases from 3 to 4 and then to 6, the received voltage correspondingly rises from 1.78 to 2.40 and 3.56 V, respectively (Table S4). This increase in induced voltage leads to a higher charging rate, allowing the IWC-MSCs to reach their operating voltage more quickly and thus improving the overall energy transfer efficiency. Considering that an increased number of turns enlarges the device footprint and four turns are sufficient for induction in this system, a four-turn coil is selected as the antenna. Therefore, the optimal parameters of the WCC are 0.4 mm of the gap, 0.5 cm of the transmission distance, and 4 turns of the

coils, resulting in a receiving voltage of 2.4 V and current of 0.68 mA.

The inductance performance of the antenna is further characterized by using an alternating current impedance method (Figure 4f–i). The WCC is measured across a frequency range of 20 to 600 kHz, and key parameters including real impedance (Z'), imaginary impedance (Z''), phase angle (θ), and inductance (L) are obtained. The real impedance exhibits only minor variations across the entire frequency range, indicating that the coil resistance (149 Ω) and direct current losses remain stable, thus minimizing fluctuations in transmission efficiency (Figure 4f). It is because the antenna is made of high-conductivity Ti_3C_2 MXene, which contributes less frequency affection. In contrast, commercial metal-based antennas typically suffer from the skin effect of free electrons at higher frequencies, which leads to reduced conductivity.⁶⁸ The inductance of the WCC in Figure 4i is obtained according to the imaginary impedance shown in Figure 4g by using the formula: $L(H) = Z''(\Omega)/2\pi f$ (Hz), where L is the inductance of the WCC; Z'' is the imaginary impedance of the WCC; and f is the measured frequency. Moreover, both the phase angle and the inductance exhibit a sharp drop near 82.5 kHz (Figure 4h,i), indicating that this is the first resonant frequency of the coils. The results indicate that the charging coils, when functioning as an antenna, exhibit excellent frequency stability.⁶⁹ The wireless charging system achieves a power transfer efficiency of 51.9% (Figure S18), confirming that the fabricated MXene-based WCC operates as a reliable inductive antenna. Overall, these results highlight the potential of Ti_3C_2 MXene-based WCCs for practical energy harvesting and wireless charging applications, providing a robust platform for flexible and efficient electromagnetic devices.

3.5. Testing Performance and Application of IWC-MSCs. To evaluate the wireless charging performance of the integrated device, we conducted a more in-depth investigation into the charging and discharging capabilities of the IWC-MSCs. As shown in the circuit diagrams (Figure 1b), the wireless charging system is composed of a transmitting part and a receiving part. To facilitate the wireless charging process, the transmitter coils, which are circular coils made of copper magnet wires, are powered by a 7 V direct current (DC) source (Figure 5a). We deliberately adopted a circular coil design because it generates a more uniform and symmetric magnetic field distribution in the central region, which enhances the coupling efficiency with the MSCs located at the center.⁷⁰ The IWC-MSCs function as the receiving units and are connected to an external humidity and temperature sensor to monitor their discharging capacity (Figure 5b). The integrated wireless charging energy storage system can be readily embedded in clothing, functioning as a wearable and portable electronic device (Figure 5c). It indicates high environmental adaptability and operability. When the transmitter using a 7 V power supply is placed 0.5 cm above the receiver, the IWC-MSCs are charged by an antenna within a magnetic field. In Figure 5d, the wireless charging voltage rapidly rises to approximately 2.5 V within the first 100 s and then gradually saturates, while the inset shows the charging current initially reaches ~0.7 mA and decreases as the capacitor becomes fully charged. The inset further shows the corresponding charging current, which initially reaches ~0.7 mA and progressively decreases as the device becomes fully charged, consistent with the expected capacitor charging

process, indicating the efficient conversion of magnetic field energy into electrical energy and successful storage in the MSCs. Figure 5e illustrates the discharging profile, where the MSCs deliver a stable output voltage of around 2 V over 500 s. The inset indicates a continuous discharge current (~0.51 mA at the beginning), gradually decaying with time, confirming the reliable energy release capability of the device. After 8 min of wireless charging, the total induced charge reaches approximately 71.1 mC. Once the charging process is completed, the stored charges are released during the discharging phase. The total energy and power output of the IWC-MSCs both reach 1.23 mW, respectively. These results collectively demonstrate that the integrated IWC-MSCs can not only harvest wireless power efficiently but also store and supply it stably for practical electronic applications. The fabricated IWC-MSCs devices are further adopted as wireless power supply in wearable electronics. The real-time charging process is tested in working temperature and humidity meters (Figure 5f). There is a linear relationship between the charging time and the corresponding working time when the charging time increases from 0 to 140 s. However, when the charging time is further extended to 200 s, the working time remains constant. It suggests that the MSCs reach the balance state of charging–discharging at the 140 s mark. Specifically, after 140 s of wireless charging, the energy stored in the IWC-MSCs is sufficient to power the humidity and temperature sensor for approximately 43 min (~2600 s) (Table S5). As a result, they can effortlessly power the humidity and temperature meters as soon as the transmitter is in proximity to the receiver, directly replacing the commercial button-cell battery, as depicted in Figure 5g and Movie S1. As illustrated in Figure 5h, even when subjected to bending, the wearable system remained fully functional, highlighting the excellent flexibility and stability of the printed IWC-MSCs during dynamic operation. To explore alternative integration scenarios, we embed the IWC-MSCs into a soft-bodied doll, where the device successfully powers a red LED (light-emitting diode) indicator (Figure 5i). Similarly, when mounted on the surface of the doll (Figure 5j), the system continues to provide sufficient energy to light the LED. These demonstrations confirm the feasibility of integrating IWC-MSCs into diverse application forms, including soft robotics, smart toys, and low-power embedded electronics. The integration of wireless charging into MSCs significantly simplifies the energy supply for wearable electronics and promotes practical applications, such as serving as portable or wearable power sources.

4. CONCLUSION

In conclusion, we have developed seamlessly integrated MXene-based IWC-MSCs using a one-step extrusion printing technique that enables the monolithic coprinting of electromagnetic coils and interdigitated microsupercapacitor electrodes. This additive manufacturing strategy eliminates physical joint interfaces between functional modules, thereby significantly reducing interfacial resistance and mitigating mechanical mismatch during deformation that often compromises the performance of conventionally assembled flexible systems. By optimizing the rheological behavior of Ti_3C_2 MXene inks and the electromagnetic coupling design, our system achieves a wireless energy transfer efficiency of up to 51.9%. The resulting devices exhibit excellent electrochemical performance, including an areal capacitance of 59.36 mF cm⁻² and an energy density of 26.71 μWh cm⁻², along with outstanding mechanical

robustness. Notably, the device retains nearly 100% capacitance after 10,000 charge–discharge cycles and exhibits negligible capacitance variation under repeated bending at 90°, highlighting both electrochemical durability and mechanical flexibility for practical wearable applications. This work provides a promising pathway for the scalable fabrication of next-generation wirelessly powered energy storage systems and establishes a foundational platform for the advancement of high-performance, monolithically integrated electronics with potential applications in flexible sensing, smart textiles, and implantable medical devices.

■ ASSOCIATED CONTENT

§ Supporting Information

The Supporting Information is available free of charge at <https://pubs.acs.org/doi/10.1021/acsanm.Sc03882>.

IWC-MSCs devices for temperature and humidity meter (Movie S1) ([MP4](#))

Characterization, computational, and experimental details (Figures S1–S18); comparison of MSCs with other reported devices (Table S1); wireless power transfer performance under different input voltages and distances (Table S2); receiver-side voltage, current, power, and corresponding efficiency at different coil separation distances (Table S3); effect of coil turns on induced voltage at a fixed input voltage of 7 V (Table S4); and correlation between simultaneous charging–discharging and standalone discharging performance (Table S5) ([PDF](#))

■ AUTHOR INFORMATION

Corresponding Authors

Weiwei Zhao — State Key Laboratory of Flexible Electronics (LoFE) & Institute of Advanced Materials (IAM), Nanjing University of Posts & Telecommunications, Nanjing 210023, China; orcid.org/0000-0003-2926-8476; Email: iamwwzhao@njupt.edu.cn

Qiang Zhao — State Key Laboratory of Flexible Electronics (LoFE) & Institute of Advanced Materials (IAM) and College of Electronic and Optical Engineering & College of Flexible Electronics (Future Technology), Nanjing University of Posts & Telecommunications, Nanjing 210023, China; School of Electronics and Information Technology, Nanjing University of Information Science and Technology, Nanjing 210044, China; orcid.org/0000-0002-3788-4757; Email: iamqzhao@njupt.edu.cn

Authors

Zhen You — State Key Laboratory of Flexible Electronics (LoFE) & Institute of Advanced Materials (IAM), Nanjing University of Posts & Telecommunications, Nanjing 210023, China

Yuzhe Chen — State Key Laboratory of Flexible Electronics (LoFE) & Institute of Advanced Materials (IAM), Nanjing University of Posts & Telecommunications, Nanjing 210023, China

Xiaoyuan Jia — State Key Laboratory of Flexible Electronics (LoFE) & Institute of Advanced Materials (IAM), Nanjing University of Posts & Telecommunications, Nanjing 210023, China

Xueqing Chen — State Key Laboratory of Flexible Electronics (LoFE) & Institute of Advanced Materials (IAM), Nanjing

University of Posts & Telecommunications, Nanjing 210023, China

Xuan Zhang — State Key Laboratory of Flexible Electronics (LoFE) & Institute of Advanced Materials (IAM), Nanjing University of Posts & Telecommunications, Nanjing 210023, China

Qiang Wang — State Key Laboratory of Flexible Electronics (LoFE) & Institute of Advanced Materials (IAM), Nanjing University of Posts & Telecommunications, Nanjing 210023, China

Ning Ding — State Key Laboratory of Flexible Electronics (LoFE) & Institute of Advanced Materials (IAM), Nanjing University of Posts & Telecommunications, Nanjing 210023, China

Shujuan Liu — State Key Laboratory of Flexible Electronics (LoFE) & Institute of Advanced Materials (IAM), Nanjing University of Posts & Telecommunications, Nanjing 210023, China

Complete contact information is available at:

<https://pubs.acs.org/10.1021/acsanm.Sc03882>

Author Contributions

Z.Y. conducted the main experiments and data analysis. Y.C. was responsible for material preparation and characterization. X.J. contributed to the electrochemical testing. X.C., X.Z., and Q.W. assisted in device fabrication and performance evaluation. N.D. participated in data analysis and manuscript editing. W.Z. supervised the experimental procedures and reviewed the manuscript. S.L. provided technical guidance and support. Q.Z. conceived and designed the project, supervised the overall research, and finalized the manuscript. All authors reviewed and approved the final version of the manuscript.

Notes

The authors declare no competing financial interest.

■ ACKNOWLEDGMENTS

This work was supported by National Natural Science Foundation of China 62174086 (W.Z.), 62474096 (W.Z.), and Outstanding Youth Foundation of Jiangsu Province (BK20240139 (W.Z.)) and funded by Basic Research Program of Jiangsu (BK20243057 (Q.Z.)) and Qinglan Project of Jiangsu Province of China (W.Z.).

■ REFERENCES

- (1) Shin, J.; Song, J. W.; Flavin, M. T.; Cho, S.; Li, S.; Tan, A.; Pyun, K. R.; Huang, A. G.; Wang, H.; Jeong, S.; et al. A non-contact wearable device for monitoring epidermal molecular flux. *Nature* **2025**, 640 (8058), 375–383.
- (2) Yang, J.; Li, M.; Fang, S.; Wang, Y.; He, H.; Wang, C.; Zhang, Z.; Yuan, B.; Jiang, L.; Baughman, R. H.; Cheng, Q. Water-induced strong isotropic MXene-bridged graphene sheets for electrochemical energy storage. *Science* **2024**, 383 (6684), 771–777.
- (3) Cheng, S.; Zhang, Z.; Yan, J.; Yang, T.; Zhang, J.; Fu, J. Revolutionizing micro-supercapacitors: Tuning MnO₂ electrode polarity and redox activity for superior energy storage. *Adv. Funct. Mater.* **2025**, 35, No. 2502526.
- (4) Xu, X.; Zhang, Z.; Zhang, Z.; Tang, X.; Chen, H.; Li, T.; Zhang, J.; Feng, Q.; Qiao, S. Metalion-bonded two-dimensional framework non-Van der Waals sandwich heterojunctions for fast mass transfer in flexible in-plane micro-supercapacitors. *eScience* **2025**, No. 100404.
- (5) Du, X.; Lu, J.; Liang, Y.; Zhang, Y.; Gao, J.; Zhu, X. Editable 3D Micro-Supercapacitor with High Energy Density Based on Mortise–Tenon Joint Structures. *ACS Appl. Mater. Interfaces* **2023**, 15 (17), 21134–21142.

- (6) Peng, X.; Peng, W.; Chen, Y.; Yan, Z.; Lee, L.; Hsiao, K.; Lu, M.; Shao, B.; Jhan, D.; Xie, B.; et al. Synergistically designed carbon-based hybrid non-contact triboelectric-and-electromagnetic nanogenerator with ultralong charge retention for wearable and ambient electromagnetic-waste energy harvesting and self-powered sensing. *Mater. Sci. Eng., R* **2025**, *165*, No. 100994.
- (7) Gao, C.; Liu, J.; Han, Y.; Chen, R.; Huang, J.; Gu, Y.; Zhao, Y.; Qu, L. An energy-adjustable, deformable, and packable wireless charging fiber supercapacitor. *Adv. Mater.* **2024**, *36* (49), No. 2413292.
- (8) Liang, Y.; Gao, J.; Wang, Q.; Lu, N.; Zhang, Y.; Zhu, X. Self-healing micro-supercapacitor based on robust liquid metal-CNT-PEDOT: PSS film for wireless powering of integrated strain sensor. *Small Methods* **2025**, *9* (4), No. 2401581.
- (9) Wang, M.; Feng, S.; Bai, C.; Ji, K.; Zhang, J.; Wang, S.; Lu, Y.; Kong, D. Ultrastretchable MXene microsupercapacitors. *Small* **2023**, *19* (21), No. 2300386.
- (10) Xie, Q.; Yi, C.; Zhang, H.; Xia, H.; Xu, G.; Miao, C.; Yang, L.; Shui, T.; Zhang, W.; Sun, Z. Stretchable Zn-Ion hybrid capacitor with hydrogel encapsulated 3D interdigital structure. *Adv. Energy Mater.* **2024**, *14* (8), No. 2303592.
- (11) Li, Q.; Wang, Q.; Li, L.; Yang, L.; Wang, Y.; Wang, X.; Fang, H. Femtosecond laser-etched MXene microsupercapacitors with double-side configuration via arbitrary on-and through-substrate connections. *Adv. Energy Mater.* **2020**, *10* (24), No. 2000470.
- (12) Yang, Z.; Wang, B.; Peng, Y.; Yuan, Y.; Tang, Z.; Meng, W.; Zhao, Y.; Wang, X. One-step sustainable preparation of laser induced S-doped graphene for assembly of high-performance supercapacitors. *J. Cleaner Prod.* **2024**, *450*, No. 141956.
- (13) Zhu, X.-D.; Ren, C.; Liang, Y.; Liang, X.; Lu, N.; Zhang, Y.; Zhao, Y.; Gao, J. Laser-assisted one-step fabrication of interlayer-spacing-regulated three-dimensional MXene-based micro-supercapacitors. *Chem. Eng. J.* **2024**, *483*, No. 149253.
- (14) Gao, C.; Huang, J.; Xiao, Y.; Zhang, G.; Dai, C.; Li, Z.; Zhao, Y.; Jiang, L.; Qu, L. A seamlessly integrated device of micro-supercapacitor and wireless charging with ultrahigh energy density and capacitance. *Nat. Commun.* **2021**, *12* (1), No. 2647.
- (15) Wang, T.; Li, C.; Xie, X.; Lu, B.; He, Z.; Liang, S.; Zhou, J. Anode materials for aqueous zinc ion batteries: mechanisms, properties, and perspectives. *ACS Nano* **2020**, *14* (12), 16321–16347.
- (16) Jing, M.; Yu, S.; Liu, Z.; Zhang, Z.; Zhang, Y.; Liu, J.; Ma, X.; Fang, D. Universal construction of novel asymmetric pseudocapacitors by poly-ILs functionalized graphene with electrochemical redox activity. *J. Energy Storage* **2025**, *113*, No. 115665.
- (17) Inman, A.; Mohammadlo, B. S.; Shevchuk, K.; FitzPatrick, J.; Park, J. W.; Pacik Nelson, N.; Roslyk, I.; Gallo, E. M.; Garg, R.; Vitale, F.; et al. MXene-enabled textile-based energy grid utilizing wireless charging. *Mater. Today* **2024**, *81*, 59–69.
- (18) Liang, Y.; Gao, J.; Shen, T.; Lu, N.; Mu, T.; Zhang, Y.; Zhu, X. Liquid metal-transition metal oxide photoactive electrode with interfacial interlocking structure for photo-enhanced asymmetric micro-supercapacitor. *Chem. Eng. J.* **2025**, *515*, No. 163698.
- (19) Zhao, W.; Peng, J.; Wang, W.; Jin, B.; Chen, T.; Liu, S.; Zhao, Q.; Huang, W. Interlayer hydrogen-bonded metal porphyrin frameworks/MXene hybrid film with high capacitance for flexible all-solid-state supercapacitors. *Small* **2019**, *15* (18), No. 1901351.
- (20) Kim, Y.; Gu, G. H.; Seol, J. B.; Kim, H. S. Multi-scale design of deformation mechanisms at hetero-zone boundaries: Dual HDI strengthening driven by TRIP effect. *J. Mater. Sci. Technol.* **2025**, *232*, 123–138.
- (21) Ren, C.-Y.; Qiu, S.; Zhai, J.; Zhang, K.; Lu, J.; Gao, J.; Wang, C.; Zhang, Y.; Zhu, X. Ionic liquid-wrapped MXene film with bowl-like structures for highly integrated micro-supercapacitor array with ultrahigh output voltage. *Nano Res.* **2023**, *16* (4), 4926–4932.
- (22) Xu, Y.; Wu, B.; Hou, C.; Li, Y.; Wang, H.; Zhang, Q. Reconfigurable flexible thermoelectric generators based on all-inorganic MXene/Bi₂Te₃ composite films. *FlexMat* **2024**, *1* (3), 248–257.
- (23) Shao, Y.; Wei, L.; Wu, X.; Jiang, C.; Yao, Y.; Peng, B.; Chen, H.; Huangfu, J.; Ying, Y.; Zhang, C. J.; Ping, J. Room-temperature high-precision printing of flexible wireless electronics based on MXene inks. *Nat. Commun.* **2022**, *13* (1), No. 3223.
- (24) Ren, Z.; Shi, X.; Yang, Q.; Li, C.; Liu, H.; Bai, T.; Ma, Y.; Das, P.; Liu, H.; Yang, E.; et al. An ultrastretchable seamlessly integrated contactless charging microsystem towards skin-attachable wireless microelectronics. *Nat. Commun.* **2025**, *16* (1), No. 1642.
- (25) Liu, M.; Zhang, H.; Huang, X.; Zhang, Z.; Zhang, K.; Chen, Z.; Zhou, J.; Pan, L. An electric-magnetic dual-gradient composite film comprising MXene, hollow Fe₃O₄, and bacterial cellulose for high-performance EMI shielding and infrared camouflage. *Adv. Funct. Mater.* **2025**, *35*, No. 2419077.
- (26) Dutta, A.; Porat, H.; Goldreich, A.; Yadgarov, L.; Kafizas, A.; Shpigel, N.; Borenstein, A. Laser exfoliated 2D MXene for supercapacitor applications. *Chem. Eng. J.* **2024**, *500*, No. 157342.
- (27) Gao, C.; You, Q.; Huang, J.; Sun, J.; Yao, X.; Zhu, M.; Zhao, Y.; Deng, T. Ultraconformable integrated wireless charging micro-supercapacitor skin. *Nano-Micro Lett.* **2024**, *16* (1), No. 123.
- (28) Lee, S. S.; Kim, S. H.; Ahn, D. B.; Lee, K. H.; Jo, Y.; Jeong, S.; Lee, S. Y. All-direct-ink-writing of artistic supercapacitors: toward on-demand embodied power sources. *Adv. Funct. Mater.* **2022**, *32* (34), No. 2202901.
- (29) Dai, Y.; Wu, X.; Li, L.; Zhang, Y.; Deng, Z.; Yu, Z.; Zhang, H. 3D printing of resilient, lightweight and conductive MXene/reduced graphene oxide architectures for broadband electromagnetic interference shielding. *J. Mater. Chem. A* **2022**, *10* (21), 11375–11385.
- (30) Baig, M. M.; Khan, S. A.; Ahmad, H.; Liang, J.; Zhu, G.; Pang, H.; Zhang, Y. 3D printing of hydrogels for flexible micro-supercapacitors. *FlexMat* **2024**, *1* (1), 79–99.
- (31) Zhao, W.; Ni, H.; Ding, C.; Liu, L.; Fu, Q.; Lin, F.; Tian, F.; Yang, P.; Liu, S.; He, W.; et al. 2D Titanium carbide printed flexible ultrawideband monopole antenna for wireless communications. *Nat. Commun.* **2023**, *14* (1), No. 278.
- (32) Guo, B.; Liang, G.; Yu, S.; Wang, Y.; Zhi, C.; Bai, J. 3D printing of reduced graphene oxide aerogels for energy storage devices: a paradigm from materials and technologies to applications. *Energy Storage Mater.* **2021**, *39*, 146–165.
- (33) Ho, M.; Ramirez, A. B.; Akbarnia, N.; Croiset, E.; Prince, E.; Fuller, G. G.; Kamkar, M. Direct ink writing of conductive hydrogels. *Adv. Funct. Mater.* **2025**, *35*, No. 2415507.
- (34) Wang, C.; Zhao, Z.; Li, Z.; Jia, Y.; Sharma, A. A.; Zhang, X. S. Direct ink writing of magnetic soft materials with optimized printing path. *Addit. Manuf.* **2025**, *105*, No. 104770.
- (35) Duan, Z.; Hu, C.; Liu, W.; Liu, J.; Chu, Z.; Yang, W.; Li, L.; Shen, G. An all-MXene-based flexible, seamless system with integrated wireless charging coil, micro-supercapacitor, and photodetector. *Adv. Mater. Technol.* **2023**, *8* (15), No. 2300157.
- (36) Niu, S.; Matsuhisa, N.; Beker, L.; Li, J.; Wang, S.; Wang, J.; Jiang, Y.; Yan, X.; Yun, Y.; Burnett, W.; et al. A wireless body area sensor network based on stretchable passive tags. *Nat. Electron.* **2019**, *2* (8), 361–368.
- (37) Zhang, L.; Qin, J.; Das, P.; Wang, S.; Bai, T.; Zhou, F.; Wu, M.; Wu, Z. Electrochemically exfoliated graphene additive-free inks for 3D printing customizable monolithic integrated micro-supercapacitors on a large scale. *Adv. Mater.* **2024**, *36* (19), No. 2313930.
- (38) Ma, J.; Qin, J.; Zheng, S.; Fu, Y.; Chi, L.; Li, Y.; Dong, C.; Li, B.; Xing, F.; Shi, H.; Wu, Z. S. Hierarchically structured Nb₂O₅ microflowers with enhanced capacity and fast-charging capability for flexible planar sodium ion micro-supercapacitors. *Nano-Micro Lett.* **2024**, *16* (1), No. 67.
- (39) Zhu, Q.; Zhao, D.; Cheng, M.; Zhou, J.; Owusu, K. A.; Mai, L.; Yu, Y. A new view of supercapacitors: integrated supercapacitors. *Adv. Energy Mater.* **2019**, *9* (36), No. 1901081.
- (40) Li, S.; Cao, P.; Li, F.; Asghar, W.; Wu, Y.; Xiao, H.; Liu, Y.; Zhou, Y.; Yang, H.; Zhang, Y.; et al. Self-powered stretchable strain sensors for motion monitoring and wireless control. *Nano Energy* **2022**, *92*, No. 106754.

- (41) Sheng, X.; Du, Z.; Gao, Z.; Xu, J.; Li, L.; Shen, G. An implantable in-hydrogel wireless supercapacitor-activated neuron system enables bidirectional modulation. *Adv. Mater.* **2025**, *37*, No. 2504558.
- (42) Shi, D.; Yang, M.; Zhang, B.; Ai, Z.; Hu, H.; Shao, Y.; Shen, J.; Wu, Y.; Hao, X. BCN-assisted built-in electric field in heterostructure: an innovative path for broadening the voltage window of aqueous supercapacitor. *Adv. Funct. Mater.* **2022**, *32* (12), No. 2108843.
- (43) Javed, M. S.; Najam, T.; Hussain, I.; Idrees, M.; Ahmad, A.; Imran, M.; Shah, S. S. A.; Luque, R.; Han, W. Fundamentals and scientific challenges in structural design of cathode materials for zinc-ion hybrid supercapacitors. *Adv. Energy Mater.* **2023**, *13* (3), No. 2202303.
- (44) Scidà, A.; Haque, S.; Treossi, E.; Robinson, A.; Smerzi, S.; Ravesi, S.; Borini, S.; Palermo, V. Application of graphene-based flexible antennas in consumer electronic devices. *Mater. Today* **2018**, *21* (3), 223–230.
- (45) Ahmed, A.; Sharma, S.; Adak, B.; Hossain, M. M.; LaChance, A. M.; Mukhopadhyay, S.; Sun, L. Two-dimensional MXenes: New frontier of wearable and flexible electronics. *InfoMat* **2022**, *4* (4), No. e12295.
- (46) Wan, S.; Chen, Y.; Huang, C.; Huang, Z.; Liang, C.; Deng, X.; Cheng, Q. Scalable ultrastrong MXene films with superior osteogenesis. *Nature* **2024**, *634* (8036), 1103–1110.
- (47) Zhou, Y.; Li, J.; Fu, H.; Li, N.; Chai, S.; Duan, T.; Xu, L.; Wang, Z.; Xu, J. Additive-free $Ti_3C_2T_x$ MXene/carbon nanotube aqueous inks enable energy density enriched 3D-printed flexible micro-supercapacitors for modular self-powered systems. *Carbon Energy* **2025**, *7* (4), No. e698.
- (48) Wang, W.; Wen, J.; Hou, X.; Zhang, Y.; Ye, W.; Wang, S.; Zhao, R.; Xue, W. Enhanced microwave absorption of superlattice C-CuS/MXene composites with rich heterogeneous interfaces and conductive network synergies. *Mater. Today Phys.* **2023**, *35*, No. 101108.
- (49) Zhao, W.; Jiang, M.; Wang, W.; Liu, S.; Huang, W.; Zhao, Q. Flexible transparent supercapacitors: materials and devices. *Adv. Funct. Mater.* **2021**, *31* (11), No. 2009136.
- (50) Chen, S.; Qiu, L.; Cheng, H. Carbon-based fibers for advanced electrochemical energy storage devices. *Chem. Rev.* **2020**, *120* (5), 2811–2878.
- (51) Satpathy, S.; Misra, N. K.; Kumar Shukla, D.; Goyal, V.; Bhattacharyya, B. K.; Yadav, C. S. An in-depth study of the electrical characterization of supercapacitors for recent trends in energy storage system. *J. Energy Storage* **2023**, *57*, No. 106198.
- (52) Cai, R.; Liang, C.; Duan, Y.; Zhao, Z.; Zhang, X.; He, P.; Yang, J.; Lai, W.; Wei, J.; Tian, L. Metallic nanoparticle inks for flexible printed electronics. *FlexMat* **2025**, *2* (2), 225–283.
- (53) Uzun, S.; Schelling, M.; Hantanasirisakul, K.; Mathis, T. S.; Askeland, R.; Dion, G.; Gogotsi, Y. Additive-free aqueous MXene inks for thermal inkjet printing on textiles. *Small* **2021**, *17* (1), No. 2006376.
- (54) Ma, R.; Chen, Z.; Zhao, D.; Zhang, X.; Zhuo, J.; Yin, Y.; Wang, X.; Yang, G.; Yi, F. $Ti_3C_2T_x$ MXene for electrode materials of supercapacitors. *J. Mater. Chem. A* **2021**, *9* (19), 11501–11529.
- (55) Kim, H. H.; Cho, Y. D.; Baek, D.; Rho, K. H.; Park, S. H.; Lee, S. Parallelization of microfluidic droplet junctions for ultraviscous fluids. *Small* **2022**, *18* (48), No. 2205001.
- (56) Xie, B.; Wang, Y.; Lai, W.; Lin, W.; Lin, Z.; Zhang, Z.; Zou, P.; Xu, Y.; Zhou, S.; Yang, C.; et al. Laser-processed graphene based micro-supercapacitors for ultrathin, rollable, compact and designable energy storage components. *Nano Energy* **2016**, *26*, 276–285.
- (57) Abdulhamid, Z. M.; Lokhande, A.; Pasanaje, A. H.; Choi, D.; Singh, N.; Polychronopoulou, K.; Anjum, D. H. Highly boosted energy storage performance of few-layered MoS₂ utilized for improved electrode fabrication: experimental and theoretical studies. *J. Mater. Chem. A* **2024**, *12* (23), 13946–13959.
- (58) Roscow, J. I.; Bowen, C.; Almond, D. Breakdown in the case for materials with giant permittivity? *ACS Energy Lett.* **2017**, *2* (10), 2264–2269.
- (59) Liu, N.; Gao, Y. Recent progress in micro-supercapacitors with in-plane interdigital electrode architecture. *Small* **2017**, *13* (45), No. 1701989.
- (60) Liang, X.; Tang, L.; Zhang, Y.; Zhu, X.; Gao, J. Robust graphene-based aerogel for integrated 3D asymmetric supercapacitors with high energy density. *Chem. - Asian J.* **2024**, *19* (10), No. e202400243.
- (61) Sun, Y.; Gao, J.; Du, X.; Zhu, X. Rapid and precise fabrication of a three-dimensional, high-capacity, asymmetric micro-supercapacitor utilizing mortise-and-tenon joint construction. *New J. Chem.* **2025**, *49*, 14866–14873.
- (62) Shi, X.; Zhou, F.; Peng, J.; Wu, R.; Wu, Z.; Bao, X. One-step scalable fabrication of graphene-integrated micro-supercapacitors with remarkable flexibility and exceptional performance uniformity. *Adv. Funct. Mater.* **2019**, *29* (50), No. 1902860.
- (63) Hsiao, C. C.; Kasten, J.; Johnson, D.; Ngozichukwu, B.; Yoo, R. M.; Lee, S.; Erdemir, A.; Djire, A. Switchable charge storage mechanism via in situ activation of MXene enables high capacitance and stability in aqueous electrolytes. *ACS Nano* **2024**, *18* (9), 7180–7191.
- (64) Zhang, C. J.; Kremer, M. P.; Seral-Ascaso, A.; Park, S. H.; McEvoy, N.; Anasori, B.; Gogotsi, Y.; Nicolosi, V. Stamping of flexible, coplanar micro-supercapacitors using MXene inks. *Adv. Funct. Mater.* **2018**, *28* (9), No. 1705506.
- (65) Peng, Y.-Y.; Akuzum, B.; Kurra, N.; Zhao, M.; Alhabeb, M.; Anasori, B.; Kumbar, E. C.; Alshareef, H. N.; Ger, M.; Gogotsi, Y. All-MXene (2D titanium carbide) solid-state microsupercapacitors for on-chip energy storage. *Energy Environ. Sci.* **2016**, *9* (9), 2847–2854.
- (66) Zhang, C. J.; McKeon, L.; Kremer, M. P.; Park, S. H.; Ronan, O.; Seral-Ascaso, A.; Barwick, S.; Coileáin, C. Ó.; McEvoy, N.; Nerl, H. C.; et al. Additive-free MXene inks and direct printing of micro-supercapacitors. *Nat. Commun.* **2019**, *10* (1), No. 1795.
- (67) Adachi, T.; Miyara, K.; Ishii, Y. Non-contact measurement of impact load due to collision of ferromagnetic projectile based on electromagnetic induction. *Int. J. Impact Eng.* **2022**, *159*, No. 104040.
- (68) Zhang, J.; Jiang, H.; Hong, W.; Meng, Q.; Xue, Z.; Zhang, M.; Chu, P. K.; Mei, Y.; Tian, Z.; Di, Z. Ultra-flexible graphene-metal nanomembrane for wireless applications. *npj Flexible Electron.* **2025**, *9* (1), No. 27.
- (69) Wu, K.; Zhu, X.; Anderson, S. W.; Zhang, X. Electrically-shielded coil-enabled battery-free wireless sensing for underwater environmental monitoring. *Adv. Sci.* **2025**, *12* (14), No. 2570095.
- (70) Zhao, J.; Zhao, L.; Zou, Y.; Chen, T. Comparison and analysis of electromagnetic characteristics of basic structure of wireless power coil for permanent magnet motors in electric vehicles. *World Electr. Veh. J.* **2023**, *14* (8), No. 199.